Research Article | Vol. 29, No. 9 / 26 April 2021 / Optics Express 14087
Optics EXPRESS

High-speed interband cascade infrared photodetectors: photo-response saturation by a femtosecond oscillator

L. M. KRÜGER,[1,*] J. HILLBRAND,[2] J. HEIDRICH,[1] M. BEISER,[2] R. WEIH,[3] J. KOETH,[3] C. R. PHILLIPS,[1] B. SCHWARZ,[2] G. STRASSER,[2,4] AND U. KELLER[1]

[1]*Department of Physics, Institute for Quantum Electronics, ETH Zurich, CH-8093 Zurich, Switzerland*
[2]*Institute of Solid State Electronics, TU Wien, Vienna, Austria*
[3]*Nanoplus Nanosystems and Technologies GmbH, 97218 Gerbrunn, Germany*
[4]*Center for Micro- and Nanostructures, TU Wien, Vienna, Austria*
[*]*lkrueger@phys.ethz.ch*

Abstract: Interband cascade infrared photodetectors (ICIPs) combine interband optical transitions with fast intraband transport to achieve high-frequency and broad-wavelength operation at room temperature. Here we study the bias-dependent electronic impulse response of ICIPs with a mid-infrared synchronously pumped optical parametric oscillator (OPO). Since the OPO produces ultrashort 104-fs pulses, it is possible to probe the impulse response of the ICIP. From this impulse response, we identify two characteristic decay times, indicating the contribution of electron as well as hole carriers. A reverse bias voltage applied to the ICIP reduces both time scales and leads to an increased electrical cut-off frequency. The OPO emits up to 500 mW average power, of which up to 10 mW is directed to the ICIP in order to test its saturation characteristics under short-pulse illumination. The peak of the impulse response profile as well as the average photocurrent experience a gradual saturation behavior, and we determine the corresponding saturation powers by measuring the photo-response as a function of average power directed to the ICIP. We demonstrate that an increasing reverse bias increases the saturation power as well as the responsivity of the ICIP.

1. Introduction

The mid-infrared (mid-IR) wavelength-region is of great interest for many industrial and scientific applications. Trace-gas molecules exhibit strong and distinct absorption features at mid-IR wavelengths, also often referred to as the molecular fingerprint region, making it the desired region for gas sensing and frequency comb spectroscopy [1–3]. Further, reduced water absorption and Rayleigh scattering in the atmosphere make the long-wavelength region attractive for free-space optical communication and lidar [4–7]. These high-speed photonic applications create an urgent need for fast and sensitive detectors.

Today, most infrared detectors for high performance and wide spectral range applications are based on narrow bandgap Mercury Cadmium Telluride (MCT). Wavelength operation in the range of 1–30 µm can be achieved with a high quantum efficiency. However, cryogenic cooling is still widely used to improve the performance of MCTs due to their higher noise compared to near-infrared detectors. Also, the high dielectric constant of MCTs, as well as a long carrier lifetime, result in a frequency response limited to one Gigahertz (GHz) [8,9]. Further, technical challenges arise from the large thermal expansion coefficient and the demanding growth process, which compromises the spatial uniformity of the material.

Intersubband transitions in quantum well infrared photodetectors (QWIPs) based on AlGaAs/GaAs heterostructures exhibit a very short carrier lifetime in the order of few picoseconds,

#423498 https://doi.org/10.1364/OE.423498
Journal © 2021 Received 24 Feb 2021; revised 12 Apr 2021; accepted 13 Apr 2021; published 23 Apr 2021

Optics EXPRESS

making them ideal candidates for high-speed detectors with high saturation intensities [10,11]. In photoconductive QWIPs the optical transition in the quantum well occurs from a bound electron state to a quasi-bound electron state that is close to resonance with the conduction band edge of the quantum well barrier. Carriers in the upper state can be efficiently extracted by applying a bias voltage, which generates a corresponding photocurrent [12]. The high responsivity of such photoconductive detectors comes at the price of a considerable dark current, which limits the achievable signal-to-noise ratio, especially at high operating temperatures.

Dark current induced noise can be circumvented by a photovoltaic detector design, such as the quantum cascade detector (QCD) [13]. The one-directional electron transport in such a device is achieved by quantum wells with gradually increasing width. This band structure creates ladder subbands with decreasing energy, which acts as an internal potential ramp for the electrons. QCDs have nowadays demonstrated high-frequency response up to 21 GHz at room temperature operation [14]. In contrast to interband detectors, however, the spectral response of an intersubband detector is relatively narrow, which is a consequence of the joint density of states of intersubband transitions [15].

The availability of high-quality antimonide (Sb) based semiconductor materials grown with molecular beam epitaxy (MBE) fueled the development of narrow bandgap detectors based on type-II superlattices (T2SLs) [16–19]. In such detectors, a type-II superlattice (T2SL) consisting of InAs quantum wells and GaSb barriers acts as an absorber. Due to the type-II broken-gap alignment between InAs and GaSb, the bandgap of the superlattice can be tailored from semimetal to small bandgap semiconductor by changing the thickness of the InAs and GaSb layers. For applications at room temperature, the short carrier lifetime and diffusion length in T2SLs introduce a constraint on the maximum absorber thickness and therefore the achievable absorption efficiency [20]. By using novel designs based on a multiple-stage (cascade) architecture [21,22], i.e., an interband cascaded infrared photodetector (ICIP) design, the absorber thickness limitation can be overcome and high-speed operation can be achieved. Such ICIPs share many physical characteristics with interband cascade lasers (ICLs) [23–25], and hence stand to complement and benefit from the advancement of ICL technology. Such ICLs are promising mid-IR sources that combine the advantages of diode lasers and quantum cascade lasers. ICLs make use of a long upper-state lifetime of optical interband transitions with the cascading principle of QCLs via fast intersubband carrier injection and extraction. Wavelength operation up to 16 µm [26], as well as the formation of frequency combs [27,28] and even picosecond pulses have been demonstrated [29]. The strongly reduced nonradiative recombination rate in the QW compared to quantum cascade lasers reduced the threshold current density by an order of magnitude.

Also, ICLs offer an attractive platform for the monolithic integration of emitters and detectors. The very same epitaxial material can be operated as a laser in forward bias and as a high-speed detector at zero or reverse bias, which provides a promising technology for on-chip communication as well as compact and energy-efficient frequency comb spectroscopy [28,30–32]. The fast frequency response of ICIPs has been characterized with high speed modulated continuous wave lasers and optical heterodyning revealing a bias-dependent response up to 7 GHz [32–35]. The low powers involved in these continuous wave investigations, however, did not reveal any saturation effects.

In this paper we present the first temporal characterization of an ICIP with a femtosecond synchronously pumped optical parametric oscillator, revealing a bias-dependent fast and slow time-constant of the photo-response, as well as its saturation characteristics. Section 2 discusses the working principle and band structure of ICIPs and section 3 describes the measurement setup. The results are presented in section 4 before we discuss observed transport and saturation behavior. Band structure simulation presented in section 5 indicate that the increased photo-response is likely caused by the alignment of the hole extractor.

Optics EXPRESS

2. Interband cascade infrared photodetector design

Interband cascade laser (ICL) structures can be used for the detection of mid-IR radiation by operating them either at zero or reverse bias [28,30,31]. The ICIP investigated in this paper is based on an ICL gain structure in order to elaborate the potential for high-speed integrated photonics applications. One stage of the ICIP active region consists of three parts, an optically active structure, a hole extractor, and an electron extractor forming one stage of the active section. In Fig. 1(a) we show a section of the electronic band structure with the relevant electron and hole states in the absence of an applied bias. The influence of applied bias will be presented in section 5. The active region is based on W-quantum wells (W-QW), consisting of one GaInSb hole quantum well sandwiched by two InAs electron quantum wells. This design enhances the electron-hole wavefunction overlap, while simultaneously suppressing Auger recombination losses [36]. The electron extractor consists of five InAs/AlSb-QWs of varying width, resulting in the formation of an electron miniband. Additionally, the electron extractor acts as a large potential barrier for the hole carriers, enforcing unidirectional carrier transport. Equivalently, a hole extractor is formed by two GaSb/AlSb hole quantum wells.

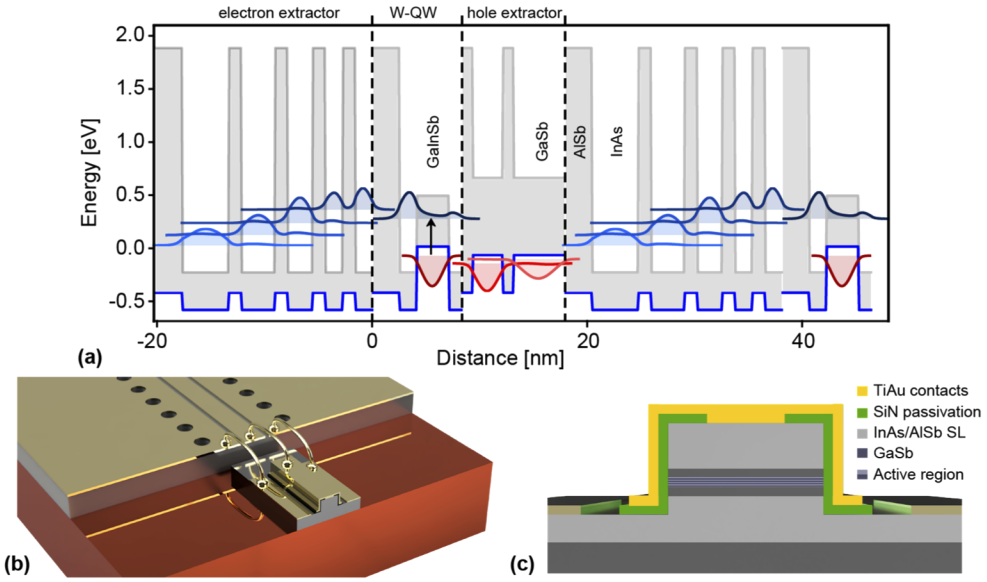

Fig. 1. (a) Simulated electronic band structure of one and a half stages of the ICIP active region, consisting of a W-quantum well (W-QW), electron extractor, and hole extractor. The relevant electron (blue) and hole (red) states are shown. (b) Illustration of an ICIP embedded in a dielectric waveguide. The ICIP is bonded to a 50-Ohm coplanar waveguide mounted on a copper substrate. (c) Front view showing the epitaxial segments as well as the waveguide structure of the ICIP.

ICLs exploit the broken-gap alignment between InAs of the electron injector and GaSb of the hole injector. At this semimetallic interface electron-hole pairs are generated internally [37]. Analogously to QCLs, this cascaded active region ensures an enhanced slope efficiency. Parameters like threshold power and output power are critically influenced by the number of stages in an ICL. Typical performance-optimized ICLs contain between 5 to 10 stages [38].

When the ICL is operated as a detector, however, the cascading scheme causes the maximum responsivity to be inversely proportional to the number of stages in the active region. This leads to a reduced external quantum efficiency of such detector structures. Nonetheless, such multi-stage detector architecture proved to be highly beneficial for high-speed detection and

Optics EXPRESS

room-temperature operation with high sensitivity [21]. A tradeoff between signal strength and thermal noise emerges if identical stages are used. The ICIP used for this work consists of four stages.

The ICIP was grown by MBE on a GaSb substrate and processed as dielectric waveguide detector, as shown in Figs. 1(b) and 1(c). To this end, 7 µm wide and 50 µm long ridges are defined using Chlorine-based reactive ion etching (RIE) with an etching depth was 3 µm. Subsequently, a SiN passivation layer is deposited around the sidewalls of the ridge by plasma-enhanced chemical vapor deposition (PECVD). The thickness of the SiN layer is 1.5 µm to reduce the parasitic capacitance of the detector. TiAu top and ground contacts are deposited by sputtering. The vertical confinement of the waveguide mode is ensured by embedding the active region into two superlattice claddings. After cleaving and top coating, the waveguide measures 36 µm in length and has a width of 7 µm. Finally, the ridge waveguide is connected via wire bonding to a coplanar 50-Ohm waveguide. The bonds were kept as short as possible (< 1 mm) to avoid parasitic inductance.

3. Saturation measurement setup

The ICIP was illuminated with a pulsed optical parametric oscillator (OPO) (Radiantis Oria IR XT) that was pumped by a Ti:sapphire mode-locked laser (Coherent Chameleon Ultra II). The spectral response of the ICIP reaches from 1.6 µm up to 3.6 µm (measured with Bruker Vertex 70v FTIR and a globar broadband mid-IR source). For the experiments presented in this paper, the idler was tuned to 2.4 µm, allowing the use of high-performance extended InGaAs photodetectors for power calibration. The OPO full-width at half maximum (FWHM) pulse duration is 104 fs based on an intensity autocorrelation assuming a sech^2 pulse shape. The optical spectrum has a FWHM bandwidth of 74 nm. The OPO has a maximum output power of ~500 mW, a pulse repetition rate of 80.2 MHz (see Fig. 2), and the beam quality factor of the idler is $M^2 = 1.4$.

The incident power on the ICIP was controlled and monitored using a variable attenuator consisting of a rotatable wire grid polarizer (Thorlabs WP25M-UB) and a fixed one transmitting only the polarization perpendicular to the growth direction of the ICIP. A reflection from the wedge was chopped at 50 Hz and detected with an integrating sphere photo detector in combination with a lock-in amplifier (LIA) for accurate monitoring of the incident power on the ICIP. A short aspheric focal length of 3 mm (Thorlabs C093TME-D) was used to couple into the ICIP ridge waveguide mounted on a high precision three-axis stage.

A bias tee separates the electronic photo-response into a constant DC part and a modulated RF part. A low-noise current preamplifier (Stanford Research SR570) transforms the generated direct current into voltage that was then detected with a voltmeter, while simultaneously controlling the applied bias voltage of the ICIP. The RF part of the signal was either analyzed in the time domain with a fast sampling oscilloscope (CSA 803 with a SD-32 50 GHz sampling head) or in the frequency domain with a 50-GHz microwave spectrum analyzer (Agilent 8565EC). The trigger signal for the oscilloscope was obtained by detecting the signal pulses of the OPO at 1.2 µm with a standard 5-GHz InGaAs fiber-coupled photodiode (Thorlabs DET08CFC).

The coupling efficiency into the waveguide mode is difficult to evaluate exactly. In contrast to passive waveguide devices there is no transmitted beam which could be used for coupling efficiency estimations. In principle the coupling efficiency can be predicted via a modal overlap integral, however this would require knowledge of the $M^2 = 1.4$ idler wavefront at the focal plane, which is not known. In lieu of a precise coupling efficiency characterization, we obtain an estimate as follows.

Coupling into the waveguide was optimized at very low average powers below one mW, measured before the focusing lens, to avoid saturation of the photo-response. We measured the transmission through the lens to be 81% and the transmission at 2.4 µm of the uncoated ICIP facet is about 70%. Therefore, the power inside the ridge waveguide is 0.56 times the power measured

Optics EXPRESS

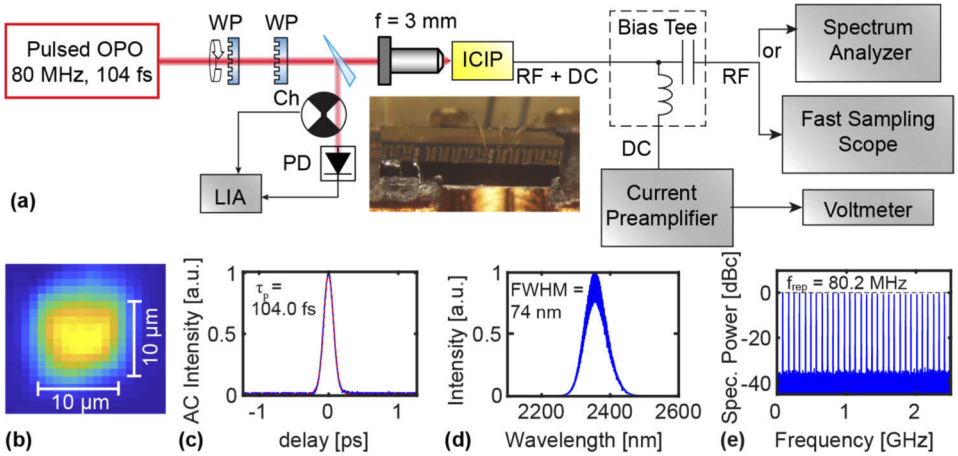

Fig. 2. (a) Experimental setup: A femtosecond OPO was used to characterize the fast response of the interband cascade infrared detector (ICIP). The incident power was adjusted by rotating the first of the two wire grid polarizers (WP). The horizontally polarized light was coupled with a short focal length lens into the 7 µm × 3 µm ridge waveguide facet. A chopped reflection from a wedge before the waveguide was used to monitor the incident power using a Lock-In Amplifier (LIA). A bias tee was used to separate the slowly varying direct current (DC) and the instantaneous radio frequency (RF) part of the electronic response. A current preamplifier was used for the DC detection and to apply a bias voltage to the ICIP. The RF signal was either analyzed with a fast sampling or by a spectrum analyzer. (b) Mapping of the focal spot using a piezo translation stage. (c) Autocorrelation (d) Optical spectrum and (e) Radiofrequency spectrum showing first 30 harmonics of the OPO pulse repetition rate.

before the focusing lens. This ratio can only be achieved under perfect coupling condition. In the limit of a single mode waveguide that would imply perfect modal overlap. For a multi-mode waveguide with a large detector facet that would require the focal spot to be smaller than the aperture of the waveguide detector.

The focal spot was mapped by translating the waveguide in 1 µm steps in the focal plane using the piezo motors of the high precision stage [Fig. 2(b)]. The $M^2 = 1.4$ idler wavefront leads to an asymmetric focal spot. The focal spot has an approximate width of 10 µm (full-width-half-maximum of Gaussian distribution fitted to photo-response in vertical and horizontal direction). An estimate for the modal overlap can be obtained from the ratio of the waveguide area and the focal spot size. With an assumed waveguide facet of 7 µm x 3 µm we obtain a modal overlap estimate of 18%, leading to an overall coupling efficiency of approximately 10% (ratio of power inside the waveguide and power before the focusing lens). The maximum peak power of the OPO pulses is 53 kW, which is 10^5 times higher than the average power (500 mW). This high peak power enabled us to reach high peak intensities of a few MW/cm^2 inside the ICIP, thereby revealing its saturation behavior for the first time.

4. Experimental results

The electronic response of the ICIP was measured at average powers incident on the focusing lens up to 10 mW and bias voltages ranging from 0 V to -3 V (reverse bias).

4.1. Saturation

The saturation behavior of multiple quantum well structures as well as T2SL has been studied extensively [18,39–41]. Empirically, the absorption coefficient decreases with increasing

Optics EXPRESS

intensities because of the depletion of available carriers in the two-dimensional quantum wells. We define a saturation power P_{sat} as the power at which the absorption is reduced to half of its initial low-power absorption α_0 according to a very simple model equation:

$$\alpha(P) = \frac{\alpha_0}{1 + \frac{P}{P_{sat}}} \tag{1}$$

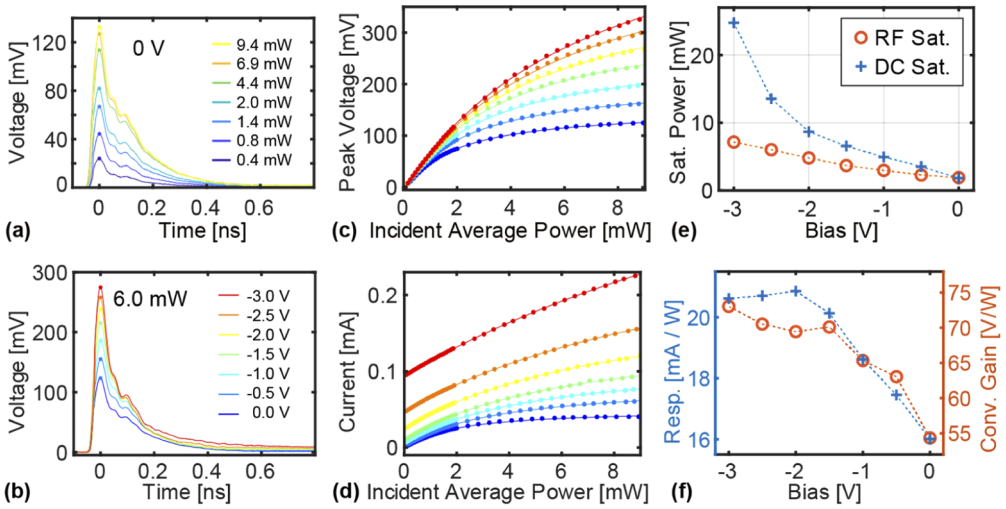

Fig. 3. (a) Power-dependent temporal response of the unbiased interband cascade infrared photodetector (ICIP). The signal-to-noise ratio was improved by averaging 128 consecutive traces for each power value. The peak voltage occurs at time zero and is marked with an additional dot in the same color as the trace. (b) Bias-dependent temporal response at an incident average power of 6.0 mW. The applied reverse bias ranges from 0 V (blue curve) to -3 V (red curve). (c) Generated peak voltage and (d) Photocurrent as a function of incident average power and applied bias. The same color solid lines represent the fitted saturation curves. (e) Fitted saturation power to RF voltage response (orange circles) and DC photocurrent (blue crosses). (f) The fitted responsivity of DC photocurrent response (blue crosses) as well as maximum conversion gain of the voltage RF response.

As the absorption starts to reduce with increasing incident power the generated electrical response saturates. The electrical signal is composed of two components: The time-dependent photo-response (RF signal) and the time-integrated total photocurrent (DC signal). In our measurements, we split the RF signal from the DC signal with a bias tee. We observe that the generated peak voltage, as well as the constant photocurrent, increases with growing incident power and higher reverse bias as shown Figs. 3(a) and 3(b), correspondingly. While we expect the peak voltage of the RF signal to be offset-free [Fig. 3(c)], the applied bias causes a dark current even if the detector is not illuminated. This dark current does not depend on the incident light and therefore leads to a constant offset in the DC signal [Fig. 3(d)]. To quantify the observed macroscopic saturation behavior of our ICIP we therefore use the following simplified phenomenological model to fit the saturation behavior in generated peak voltage and current:

$$V_{peak}(V_{bias}, P_{in}) = \frac{\alpha_{0,peak}(V_{bias}) \cdot P_{in}}{1 + \frac{P_{in}}{P_{sat,\,peak}(V_{bias})}} \tag{2}$$

$$I(V_{bias}, P_{in}) = \frac{\alpha_{0,DC}(V_{bias}) \cdot P_{in}}{1 + \frac{P_{in}}{P_{sat,DC}(V_{bias})}} + I_{Dark}(V_{bias}) \tag{3}$$

Optics EXPRESS

The measured peak voltage and DC photocurrent (colored dots), as well as the fitted saturation curves (solid lines), are shown in Figs. 3(c) and 3(d) for the bias voltage ranging from 0 V (blue curve) to -3 V (red curve). The fitted saturation powers are shown in Fig. 3(e). We observe that the saturation power of both signals, RF as well as DC, grow significantly with increasing reverse bias. However, the DC saturation $P_{\mathrm{sat,DC}}(V_{\mathrm{bias}})$ power increases stronger with reverse bias than the RF saturation power $P_{\mathrm{sat,\ peak}}(V_{\mathrm{bias}})$.

The responsivity, as well as the dark current were obtained by fitting a linear function to the photocurrent generated in the linear detector regime of average incident powers from 0.1 to 0.8 mW, well below the saturation power. Equivalently we determine the maximum conversion gain, defined as the generated voltage per average input power, for the RF signal. Responsivity and conversion gain both increase with negative reverse bias. We observed a significant increase up to an applied voltage of about -1.5 V followed by a slower increase or even reduction in the case of responsivity. This behavior indicates that the carrier extraction mechanism significantly improves with applied reverse bias.

The characteristic bias-dependent detector quantities are summarized in Table 1. As seen in Table 1 the RF saturation power increases from 1.9 mW at zero bias up to 7.2 mW at -3.0 V. The corresponding saturation pulse energy increases from 24 pJ to 90 pJ. The increased detector response and saturation power come at the cost of an increased dark current.

4.2. Fast and slow detector response

An absorbed photon in the active region of a detector creates an electron-hole pair. While this process occurs instantaneously, the carriers need to be extracted from the active region and transported to the electronic contacts of the detector, to generate an electric response. In this section, we extract two characteristic response times and study the influence of applied reverse bias.

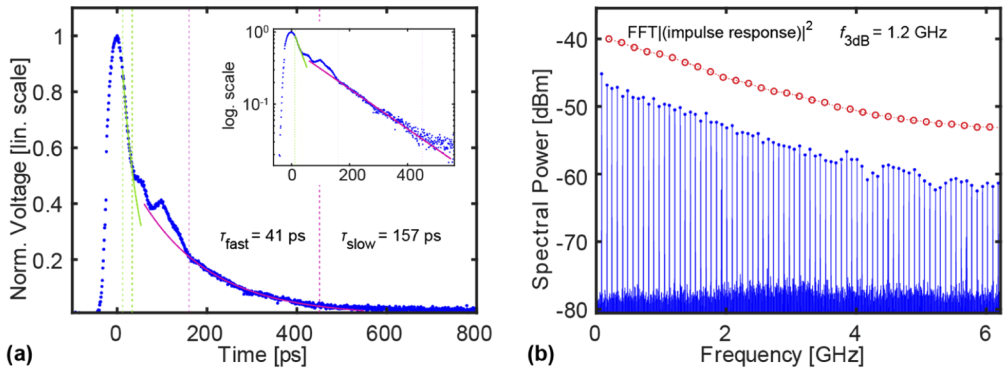

Fig. 4. ICIP temporal and frequency response at 1 mW average input power and zero bias. (a) the temporal response shows a short initial exponential decay (green interval), with a fitted decay time of 41 ps, is followed by a slower second decay characterized by a decay time of 157 ps. The insert shows the temporal response on a semilogarithmic scale. (b) Blue: measured frequency response showing the harmonics of the OPO. Red: Fourier spectrum of the temporal response; the estimated 3-dB bandwidth is 1.2 GHz.

The fast electronic ICIP response at zero bias and an incident average power of 1 mW is shown in Fig. 4. The average power is low enough to avoid significant saturation effects while maintaining a good signal-to-noise ratio. The electronic response shows a fast and slow exponential decay. The semilogarithmic representation of the electronic response shows two linear regions with a slope proportional to the exponential decay time. By fitting an exponential decay in the interval of 12 ps to 33 ps after the maximum voltage (indicated by green dotted vertical lines), occurring

Optics EXPRESS

at time zero, we extract a fast decay time of 41 ps. Equivalently, we extract a slower decay time of 157 ps in the interval of 160 ps to 450 ps (purple dotted vertical lines). The pulse duration of the incident pump pulses is at least two orders of magnitude shorter than the shortest resolved time constant. Therefore, the shape of the pump pulse cannot be resolved electronically and the measured electronic response corresponds to the impulse response of the device.

In addition, we measure the voltage response in the frequency domain with a microwave spectrum analyzer [Fig. 4(b)]. The periodic pulse train samples the frequency response of the ICIP at 80.2 MHz. The measured frequency response shows some ripples that are likely caused by electronic signal reflections in the cables as well as the wire bonding of the detector. For comparison, the calculated absolute square of the Fourier components from the measured temporal response is shown in Fig. 4(b) (blue circles); note, an offset has been applied for better comparability to the MSA measurement. A 3-dB power bandwidth of 1.2 GHz was calculated from the temporal response. We note that the temporal and frequency characterization are in good agreement as long as the detector is operated well below the saturation power.

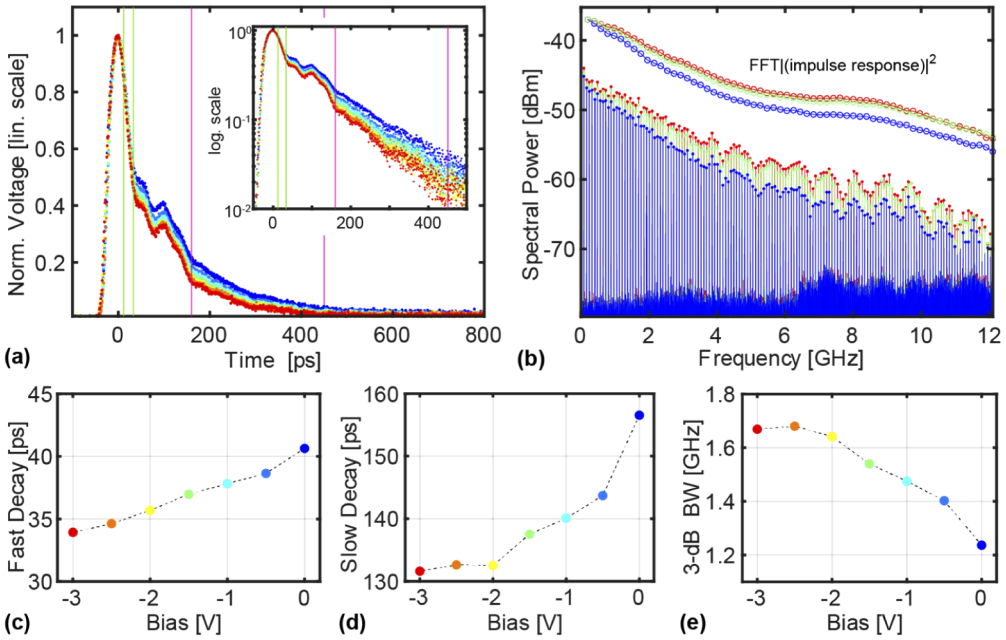

Fig. 5. (a) Electronic response measured at a fixed average input power of 1 mW for applied reverse bias from 0 V (blue) to -3 V (red). The fast decay time shown in (c) was obtained by fitting an exponential decay in the interval of [12 ps, 33 ps] (green vertical lines). Similarly, slow decay time (d) was fitted in the interval [160 ps, 450 ps]. (b) Fourier spectrum of the temporal response (circles) and corresponding measured frequency response. (e) Calculated 3-dB power bandwidth as a function of applied reverse bias.

Next, we studied the influence of reverse bias on the detector bandwidth at a fixed incident average power of 1 mW. Analogous to zero bias we fitted the fast and slow decay time in the intervals [12 ps, 33 ps] and [160 ps, 450 ps] for reverse bias ranging from 0 to -3 V [Fig. 5(a)]. The calculated frequency response is used to extract the 3-dB power bandwidth. In Fig. 5(b) we show the measured frequency response as well as the Fourier spectrum of the corresponding temporal response for applied biases of zero (blue), -1.5 V (green), and -3.0 V (red).

The fast decay time [Fig. 5(c)] decreases monotonically with increasing bias from 41 ps at zero bias to 34 ps at -3.0 V reverse bias. The slower decay time [Fig. 5(d)] decreases rapidly from

Optics EXPRESS

157 ps at zero bias to 133 ps at -2.0 V and stays approximately constant for larger reverse bias up to −3 V. Typically, one characterizes the detector speed by a 3-dB power bandwidth, defined as the frequency at which the frequency response reduces by a factor of two compared to its value at DC. We observe a considerable increase of the 3 dB bandwidth from 1.24 GHz at zero bias up to 1.68 GHz at -2.5 V and a slight decrease at -3 V. The characteristic fast and slow decay time as well as calculated 3-dB bandwidth are summarized in Table 2.

Table 1. Response and Saturation Parameters for RF and DC Signals

Bias	0.0	-0.5	-1.0	-1.5	-2.0	-2.5	-3.0
RF Conversion Gain (V/W)	54.3	63.1	65.3	70.1	69.5	70.5	73.0
DC Responsivity (mA/W)	16.0	17.5	18.6	20.1	20.8	20.7	20.6
RF Saturation Power (mW)	1.9	2.3	3.0	3.7	4.8	6.0	7.2
DC Saturation Power (mW)	1.8	3.5	5.0	6.6	8.7	13.6	24.8
Dark Current (μA)	0.44	1.95	5.93	10.0	24.5	46.5	94.0

The 3-dB bandwidth does not accurately represent the frequency response of a detector with two distinct temporal responses. This can be seen by modeling the temporal response of an ICIP as a superposition of fast and slow pulse response. The linearity of the Fourier analysis implies that the corresponding frequency response remains a superposition of two frequency responses. The initial fast temporal response in the order of 40 ps relates to a frequency response in the order of 10 GHz. In addition, the slower temporal response of 160 ps generates a frequency response at lower frequencies. In Fig. 5(b) we see a first exponential drop for frequencies above the first 3-dB point of about 1.2 GHz. At approximately 6 GHz the frequency response flattens before it drops of again for frequencies above the second 3-dB point around 9 GHz. Since detectors are typically characterized by one single 3-dB power bandwidth (defined as the frequency at which the signal drops to half of its value at DC) we calculated the first 3-dB point for the range of applied biases [see Fig. 5(e)].

Table 2. Bias Dependent Detector Response

Bias	0.0	-0.5	-1.0	-1.5	-2.0	-2.5	-3.0
Fast decay (ps)	41	39	38	37	36	35	34
Slow decay (ps)	157	144	140	138	133	133	132
Calc. 3-dB power BW (GHz)	1.24	1.40	1.48	1.54	1.64	1.68	1.67

5. Transport and saturation behavior of ICIPs

The electronic response of ICIPs is fundamentally determined by interband and intraband transitions of both photogenerated carriers. Incident radiation generates electron-hole pairs in the W-QW of the active region. Electron and holes then either escape from the W-QW in the electron and hole extractors or recombine at a rate characterized by the carrier lifetime. A long carrier lifetime in the order of nanoseconds is obtained by the W-QW design, by reducing non-radiative Auger recombination [36].

The carriers can escape the quantum well either via tunneling or thermionic emission [42,43]. Thermionic emission occurs if states above the quantum well barrier get thermally populated leading to the escape of those carriers. Therefore, the thermionic emission rate decreases exponentially with the barrier height. The temperature-insensitive tunneling rate on the other hand is determined by the tunneling barrier height and length, as well as the effective mass of the carrier in the barrier. Resonant tunneling occurs if the carrier level inside and outside of the quantum well have equal energy [44,45].

Optics EXPRESS

Escaped carriers are swept away from the quantum well by the carrier extractor section, consisting of consecutive QW governed by fast miniband transport. Subsequently, the photogenerated electron-hole pairs recombine at the semi-metallic interface (SMIF). The timescales involved in this process are however not yet fully understood. The active region is sandwiched by highly doped InAs/AlSb SL contact layers.

If only one carrier type is involved in the electronic response, a single exponential decay of the impulse response would be observed. Under the assumption that all contributing carrier transport mechanisms are independent of each other, the exponential decay rate of the impulse response is given as the sum of the individual rates. The observed double exponential decay of the impulse response therefore indicates that both carrier types are involved in the electronic response.

We suspect that the fast decay can be attributed to electrons and the slow decay to holes. The reason is threefold: First, hole carriers have a higher effective mass than electrons, which results in a decreased tunneling rate. Second, the overlap with the upper level of the QW has a larger overlap with the electron extractor state compared to its hole counterpart [Figs. 6(a)–6(d)], which leads to a greater tunneling rate. Third, the hole level at zero applied bias lies above the levels of the hole extractor [Fig. 6(e)]. As a result, the hole extraction rate of an unbiased detector is compromised. In contrast, the electron wavefunction overlaps well with the miniband of the electron extractor independent of the applied voltage bias.

When the ICIPs are reverse biased, both the fast and slow decay times are reduced leading to an increase in the frequency bandwidth. This behavior can be explained by the band structure of the lower level of the QW and the hole extractor region presented in Fig. 6. The potential difference introduced by the reverse bias shifts the energy of the electron and hole states relative to each other. In particular, the hole states are aligned in energy for a reverse bias of about −2 V [Fig. 6(g)]. This alignment of the hole injector to the hole state in the W-QW could explain the initial decrease of the slow decay time with increasing reverse bias up to -2.0 V. If the reverse bias increases even further the hole state gets pushed below the hole extractor level [Fig. 6(h)]. Under these conditions, a hole could tunnel out of the W-QW and relax subsequently to the hole extractor level. Also, we observed a continuously decreasing fast decay time with increasing reverse bias. This could be explained by efficient electron transport in the heavily doped SL as well as a reduction in effective tunneling barrier height by the applied electric field. The double exponential decay of the electronic response was also observed for OPO idler wavelengths of 2.8 µm and 3.3 µm. At both wavelengths we observed a bias dependence of the fast and slow decay as well as saturation behavior.

In addition to fundamental carrier transport timescales, the electronic detector speed is limited by the parasitic electronic components introducing a low-pass behavior. The parasitic capacitance is closely related to the detector area and minimized by the waveguide design. Parasitic inductance and resistance can be introduced by the electronic wire bond contacts and minimized by keeping them as short as possible. To estimate the RC cutoff frequency of the electronic circuit we assume that the resistance is dominated by the 50-Ohm coplanar waveguide and we approximate the ICIP capacitance by a simple plate capacitor. With these simplifications we obtain an estimated RC cutoff frequency of about 16 GHz, which is comparable to the observed faster response process observed in section 4.2. This implies that the observed faster detector response could be limited by the electronic circuit rather than the electronic transit time. Coplanar waveguide connections are elegant solutions to mitigate the circuit limitation introduced by wire-bond connections. This technique has been successfully demonstrated with QWIPs and QCDs [14,46]. Unfortunately, the high n–type doping of GaSb, required for optical transparency, prevents on-chip coplanar waveguide designs due to the large capacitance that would be formed by the conducting GaSb layer and the coplanar waveguide.

The saturation behavior of the ICIP is closely related to the carrier lifetime. The saturation power is inversely proportional to the carrier lifetime in the W-QW. The RF saturation power is

Optics EXPRESS

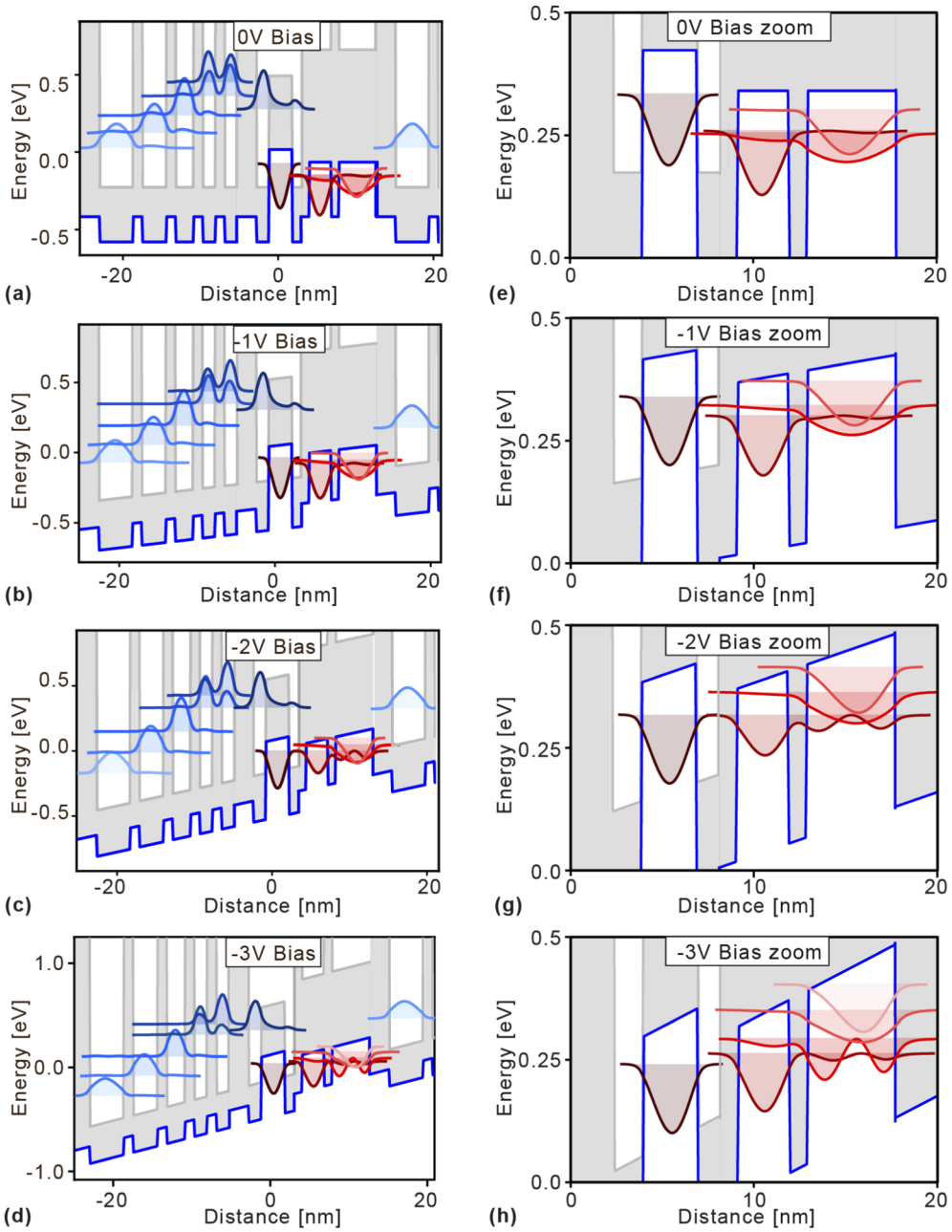

Fig. 6. Band structure simulation of one period of the ICIP active region, consisting of a W-shaped quantum well (W-QW), electron extractor, and hole extractor The relevant electron (blue) and hole (red) states are shown as a function of applied reverse bias ranging from zero (a) to -3 V (d). (e)-(h) Zoomed in image shows the hole wavefunctions in the W-QW and the hole extractor as a function of reverse bias ranging from zero to -3 V.

Optics EXPRESS

determined by the generated peak voltage whereas the DC response represents the time-integrated photo-response. We observed a strong nonlinear increase in saturation power of the DC response of the ICIP as well as an approximately linear increasing RF saturation power increasing reverse bias. A possible explanation for this behavior can be found by considering the RF saturation as an effect of carrier depletion in the W-QWs, whereas the DC saturation power is influenced by the carrier transport mechanisms. A faster carrier transport implies a higher carrier saturation power, since the generated charge pairs are extracted more efficiently from the W-QWs. Similar behavior has been observed in reverse biased quantum well systems [40,41]. The saturation behavior of ICIPs, however, requires more extensive experimental as well as theoretical investigations.

6. Conclusion

Interband cascade infrared photodetectors are promising mid-IR detectors for fast and broad wavelength detection at room temperature. The ICIP investigated in this work is based on a ICL band structure and operated at a wavelength from 1.6 µm to 3.6 µm with 3-dB bandwidth up to 1.64 GHz. We have presented the first characterization of an ICIP with a femtosecond mid-IR oscillator. Our results show that, while ICIPs can be operated under photovoltaic conditions, both the detection speed and the saturation power can be increased by applying a reverse bias underlining the potential of ICL band structures for integrated photonics applications. Moreover, the bias-dependent electronic impulse response was measured with a fast sampling scope and found to match the frequency response measured with a microwave spectrum analyzer.

We observed a double exponential decay of the impulse response indicating that both carriers contribute to the electronic response. The slow decay can likely be attributed to hole carriers for three reasons. First, the hole wavefunctions are more localized in the W-QW and have therefore less overlap with the wavefunctions of the hole extractor. Secondly, holes have a higher effective mass and thirdly the hole level lies energetically above the extractor when no bias is applied. These three effects all reduce the tunneling rate of hole carriers from the W-QW in the hole extractors.

Both decay times decrease under reverse electric bias. The faster time scale decreases linearly from 41 ps at 0 V down to 34 ps at -3 V. The longer time scale first drops rapidly from 157 ps at 0 V down to 133 ps at -2 V and stays approximately constant for values above. As a consequence, the 3-dB bandwidth increases from 1.24 GHz at zero volts up to 1.64 GHz at −2 V reverse bias. These experimental findings are further supported by our band structure simulations. At a reverse bias of about -2 V, the hole extractor is aligned to the hole level in the QW enabling efficient carrier extraction. High-frequency photovoltaic operation could be achieved by designing the hole extractor such that it is aligned to the level in the QW at zero voltage. Further, the width of the barrier between the lower state in the W-QW and the hole extractor could be reduced to improve the hole tunneling and therefore the detector speed.

Higher carrier extraction rates imply an increase in saturation power. RF saturation power increased considerably from 1.9 mW at zero bias to 7.2 mW at -3 V. Correspondingly the saturation pulse energy increased from 24 pJ to 90 pJ. Further, we observed a 28% increase in responsivity from 16.0 mA/W to 20.1 mA/W. This result has an important implication for measuring ultrashort pulses. Increasing the reverse bias not only increases the detector response but also allows for higher incident pulse energies.

The study presented in this paper reveals valuable insights into the transport timescales involved in ICIPs. Future experimental as well as theoretical investigations will lead to a deeper understanding of these complex semiconductor architectures and enable the design of next-generation high-frequency ICIPs.

Funding. European Research Council (787097, 853014); Eidgenössische Technische Hochschule Zürich (ETH-49 18-1).

Disclosures. The authors declare no conflicts of interest.

Optics EXPRESS

References

1. B. Schrader, *Infrared and Raman Spectroscopy: Methods and Applications* (John Wiley & Sons, 2008).
2. A. Schliesser, N. Picqué, and T. W. Hänsch, "Mid-infrared frequency combs," Nat. Photonics **6**(7), 440–449 (2012).
3. I. Coddington, N. Newbury, and W. Swann, "Dual-comb spectroscopy," Optica **3**(4), 414–426 (2016).
4. J. H. McElroy, N. McAvoy, E. H. Johnson, J. J. Degnan, F. E. Goodwin, D. M. Henderson, T. A. Nussmeier, L. S. Stokes, B. J. Peyton, and T. Flattau, "CO_2 laser communication systems for near-earth space applications," Proc. IEEE **65**(2), 221–251 (1977).
5. M. A. Khalighi and M. Uysal, "Survey on Free Space Optical Communication: A Communication Theory Perspective," IEEE Commun. Surv. Tutorials **16**(4), 2231–2258 (2014).
6. J. J. Liu, B. L. Stann, K. K. Klett, P. S. Cho, and P. M. Pellegrino, "Mid and long-wave infrared free-space optical communication," in *Laser Communication and Propagation through the Atmosphere and Oceans VIII* (International Society for Optics and Photonics, 2019), 11133, p. 1113302.
7. Y. Gong, L. Bu, B. Yang, and F. Mustafa, "High Repetition Rate Mid-Infrared Differential Absorption Lidar for Atmospheric Pollution Detection," Sensors **20**(8), 2211 (2020).
8. C. Verie and M. Sirieix, "Gigahertz cutoff frequency capabilities of CdHgTe photovoltaic detectors at 10.6 μ," IEEE J. Quantum Electron. **8**(2), 180–184 (1972).
9. A. Rogalski, "HgCdTe infrared detector material: history, status and outlook," Rep. Prog. Phys. **68**(10), 2267–2336 (2005).
10. H. C. Liu, J. Li, M. Buchanan, and Z. R. Wasilewski, "High-frequency quantum-well infrared photodetectors measured by microwave-rectification technique," IEEE J. Quantum Electron. **32**(6), 1024–1028 (1996).
11. P. D. Grant, R. Dudek, M. Buchanan, and H. C. Liu, "Room-Temperature Heterodyne Detection up to 110 GHz With a Quantum-Well Infrared Photodetector," IEEE Photonics Technol. Lett. **18**(21), 2218–2220 (2006).
12. H. Schneider and H. C. Liu, *Quantum Well Infrared Photodetectors - Physics and Applications* (Springer, 2007).
13. L. Gendron, M. Carras, A. Huynh, V. Ortiz, C. Koeniguer, and V. Berger, "Quantum cascade photodetector," Appl. Phys. Lett. **85**(14), 2824–2826 (2004).
14. J. Hillbrand, L. Matthieu Krüger, S. Dal Cin, H. Knötig, J. Heidrich, A. Maxwell Andrews, G. Strasser, U. Keller, and B. Schwarz, "High-speed quantum cascade detector characterized with a mid-infrared femtosecond oscillator," Opt. Express **29**(4), 5774 (2021).
15. M. Helm, "Chapter 1 The Basic Physics of Intersubband Transitions," in *Semiconductors and Semimetals*, H. C. Liu and F. Capasso, eds. (Elsevier, 1999), 62, pp. 1–99.
16. M. Razeghi and B.-M. Nguyen, "Advances in mid-infrared detection and imaging: a key issues review," Rep. Prog. Phys. **77**(8), 082401 (2014).
17. A. Rogalski, P. Martyniuk, and M. Kopytko, "InAs/GaSb type-II superlattice infrared detectors: Future prospect," Appl," Phys. Rev. **4**(3), 031304 (2017).
18. Y. Chen, Z. Xie, J. Huang, Z. Deng, and B. Chen, "High-speed uni-traveling carrier photodiode for 2 μm wavelength application," Optica **6**(7), 884–889 (2019).
19. J. Huang, Z. Xie, Y. Chen, J. E. Bowers, and B. Chen, "High Speed Mid-Wave Infrared Uni-Traveling Carrier Photodetector," IEEE J. Quantum Electron. **56**(4), 1–7 (2020).
20. D. Donetsky, G. Belenky, S. Svensson, and S. Suchalkin, "Minority carrier lifetime in type-2 InAs–GaSb strained-layer superlattices and bulk HgCdTe materials," Appl. Phys. Lett. **97**(5), 052108 (2010).
21. R. T. Hinkey and R. Q. Yang, "Theory of multiple-stage interband photovoltaic devices and ultimate performance limit comparison of multiple-stage and single-stage interband infrared detectors," J. Appl. Phys. **114**(10), 104506 (2013).
22. Y. Chen, X. Chai, Z. Xie, Z. Deng, N. Zhang, Y. Zhou, Z. Xu, J. Chen, and B. Chen, "High-Speed Mid-Infrared Interband Cascade Photodetector Based on InAs/GaAsSb Type-II Superlattice," J. Lightwave Technol. **38**(4), 939–945 (2020).
23. R. Q. Yang, "Infrared laser based on intersubband transitions in quantum wells," Superlattices Microstruct. **17**(1), 77–83 (1995).
24. C.-H. Lin, R. Q. Yang, D. Zhang, S. J. Murry, S. S. Pei, A. A. Allerman, and S. R. Kurtz, "Type-II interband quantum cascade laser at 3.8 μm," Electron. Lett. **33**(7), 598–599 (1997).
25. Z. Tian, L. Li, H. Ye, R. Q. Yang, T. D. Mishima, M. B. Santos, and M. B. Johnson, "InAs-based interband cascade lasers with emission wavelength at 10.4 μm," Electron. Lett. **48**(2), 113–114 (2012).
26. H. Lotfi, L. Li, H. Ye, R. T. Hinkey, L. Lei, R. Q. Yang, J. C. Keay, T. D. Mishima, M. B. Santos, and M. B. Johnson, "Interband cascade infrared photodetectors with long and very-long cutoff wavelengths," Infrared Phys. Technol. **70**, 162–167 (2015).
27. M. Bagheri, C. Frez, L. A. Sterczewski, I. Gruidin, M. Fradet, I. Vurgaftman, C. L. Canedy, W. W. Bewley, C. D. Merritt, C. S. Kim, M. Kim, and J. R. Meyer, "Passively mode-locked interband cascade optical frequency combs," Sci. Rep. **8**(1), 3322 (2018).
28. B. Schwarz, J. Hillbrand, M. Beiser, A. M. Andrews, G. Strasser, H. Detz, A. Schade, R. Weih, and S. Höfling, "Monolithic frequency comb platform based on interband cascade lasers and detectors," Optica **6**(7), 890–895 (2019).
29. J. Hillbrand, M. Beiser, A. M. Andrews, H. Detz, R. Weih, A. Schade, S. Höfling, G. Strasser, and B. Schwarz, "Picosecond pulses from a mid-infrared interband cascade laser," Optica **6**(10), 1334–1337 (2019).

Optics EXPRESS

30. J. V. Li, R. Q. Yang, C. J. Hill, and S. L. Chuang, "Interband cascade detectors with room temperature photovoltaic operation," Appl. Phys. Lett. **86**(10), 101102 (2005).
31. H. Lotfi, L. Li, S. M. Shazzad Rassel, R. Q. Yang, C. J. Corrége, M. B. Johnson, P. R. Larson, and J. A. Gupta, "Monolithically integrated mid-IR interband cascade laser and photodetector operating at room temperature," Appl. Phys. Lett. **109**(15), 151111 (2016).
32. L. A. Sterczewski, M. Bagheri, C. Frez, C. L. Canedy, I. Vurgaftman, and J. R. Meyer, "Mid-infrared dual-comb spectroscopy with room-temperature bi-functional interband cascade lasers and detectors," Appl. Phys. Lett. **116**(14), 141102 (2020).
33. Y. Chen, X. Zhao, J. Huang, Z. Deng, C. Cao, Q. Gong, and B. Chen, "Dynamic model and bandwidth characterization of InGaAs/GaAsSb type-II quantum wells PIN photodiodes," Opt. Express **26**(26), 35034–35045 (2018).
34. H. Lotfi, L. Li, L. Lei, H. Ye, S. M. Shazzad Rassel, Y. Jiang, R. Q. Yang, T. D. Mishima, M. B. Santos, J. A. Gupta, and M. B. Johnson, "High-frequency operation of a mid-infrared interband cascade system at room temperature," Appl. Phys. Lett. **108**(20), 201101 (2016).
35. Z. Xie, J. Huang, X. Chai, Z. Deng, Y. Chen, Q. Lu, Z. Xu, J. Chen, Y. Zhou, and B. Chen, "High-speed mid-wave infrared interband cascade photodetector at room temperature," Opt. Express **28**(24), 36915–36923 (2020).
36. J. R. Meyer, C. A. Hoffman, F. J. Bartoli, and L. R. Ram-Mohan, "Type-II quantum-well lasers for the mid-wavelength infrared," Appl. Phys. Lett. **67**(6), 757–759 (1995).
37. I. Vurgaftman, W. W. Bewley, C. L. Canedy, C. S. Kim, M. Kim, J. R. Lindle, C. D. Merritt, J. Abell, and J. R. Meyer, "Mid-IR Type-II Interband Cascade Lasers," IEEE J. Sel. Top. Quantum Electron. **17**(5), 1435–1444 (2011).
38. I. Vurgaftman, W. W. Bewley, C. L. Canedy, C. S. Kim, M. Kim, C. D. Merritt, J. Abell, and J. R. Meyer, "Interband Cascade Lasers With Low Threshold Powers and High Output Powers," IEEE J. Sel. Top. Quantum Electron. **19**(4), 1200210 (2013).
39. D. Chemla, D. Miller, P. Smith, A. Gossard, and W. Wiegmann, "Room temperature excitonic nonlinear absorption and refraction in GaAs/AlGaAs multiple quantum well structures," IEEE J. Quantum Electron. **20**(3), 265–275 (1984).
40. A. M. Fox, D. A. B. Miller, G. Livescu, J. E. Cunningham, and W. Y. Jan, "Quantum well carrier sweep out: relation to electroabsorption and exciton saturation," IEEE J. Quantum Electron. **27**(10), 2281–2295 (1991).
41. T. Sizer, T. K. Woodward, U. Keller, K. Sauer, T.-H. Chiu, D. L. Sivco, and A. Y. Cho, "Measurement of carrier escape rates, exciton saturation intensity, and saturation density in electrically biased multiple-quantum-well modulators," IEEE J. Quantum Electron. **30**(2), 399–407 (1994).
42. H. Schneider and K. V. Klitzing, "Thermionic emission and Gaussian transport of holes in a GaAs/$Al_xGa_{1-x}As$ multiple-quantum-well structure," Phys. Rev. B **38**(9), 6160–6165 (1988).
43. A. Larsson, P. A. Andrekson, S. T. Eng, and A. Yariv, "Tunable superlattice p-i-n photodetectors: characteristics, theory, and application," IEEE J. Quantum Electron. **24**(5), 787–801 (1988).
44. F. Capasso, K. Mohammed, and A. Y. Cho, "Sequential resonant tunneling through a multiquantum well superlattice," Appl. Phys. Lett. **48**(7), 478–480 (1986).
45. H. Schneider, K. von Klitzing, and K. Ploog, "Resonant and non-resonant tunneling in GaAs/AlAs multi quantum well structures," Superlattices Microstruct. **5**(3), 383–396 (1989).
46. M. Hakl, Q. Y. Lin, S. Lepillet, M. Billet, J.-F. Lampin, S. Pirotta, R. Colombelli, W. J. Wan, J. C. Cao, H. Li, E. Peytavit, and S. Barbieri, "Ultra-fast quantum-well infared photodetectors operating at 10 μm with flat response up to 70 GHz at room temperature," ArXiv200700299 Phys. (2020).